Title

Resistive Switching Memory Performance of Two-Dimensional Polyimide Covalent Organic Framework Films

Journal

ACS Applied Materials & Interfaces, 12(46)

ISSN

1944-8244

Authors

Sun, Bing

Li, Xinle

Feng, Tiantian

et al.

Publication Date

2020-11-18

DOI

10.1021/acsami.0c15789

Peer reviewed

Resistive Switching Memory Performance of Two-Dimensional Polyimide Covalent Organic Framework Films

Bing Sun,[†,‡,*] Xinle Li,[‡] Tiantian Feng,[†,§] Songliang Cai,[‡,∥] Teresa Chen,[‡] Chenhui Zhu,[⊥] Jian Zhang,[‡] Dong Wang,[§,*] Yi Liu[‡,*]

† School of Science, China University of Geosciences (Beijing), Beijing 100083, P.R. China

‡ The Molecular Foundry, Lawrence Berkeley National Laboratory, Berkeley, CA 94720, USA

§ Key Laboratory of Molecular Nanostructure and Nanotechnology, Institute of Chemistry, Chinese Academy of Sciences, Beijing 100190, P.R. China

∥ School of Chemistry, South China Normal University, Guangzhou 510006, P.R. China

⊥ Advanced Light Source, Lawrence Berkeley National Laboratory, Berkeley, CA 94720, USA

ABSTRACT: Two-dimensional polyimide covalent organic framework (2D PI-NT COF) films were constructed on indium-tin-oxide (ITO)-coated glass substrates to fabricate two-terminal sandwiched resistive memory devices. The 2D PI-NT COF films condensated from the reaction between 4,4',4''-triaminotriphenylamine and naphthalene-1,4,5,8-tetracarboxylic dianhydride under solvothermal conditions demonstrated high crystallinity, good orientation preference, tunable thickness, and low surface roughness. The well-aligned electron donor (triphenylamine unit) and acceptor (naphthalene diimide unit) arrays rendered the 2D PI-NT COF film a promising candidate for electronic applications. The memory devices based on the 2D PI-NT COF films exhibited the typical write-once-read-many-time resistive switching behavior under the operating voltage of +2.30 V on the positive scan and –2.64 V on the negative scan. A high ON/OFF current ratio (>10^6 for the positive scan and 10^4~10^6 for the negative scan) and long-term retention time indicated the high fidelity, low error, and high stability of the resistive memory devices. The memory behavior was attributed to an electric field-induced intramolecular charge transfer in the ordered donor-acceptor system which provided the effective charge transfer channels for injected charge carriers. This work represents the first example that explores the resistive memory properties of 2D PI-COF films, shedding light on the potential application of 2D COFs as information storage media.

KEYWORDS: *2D covalent organic framework film, electric field-induced charge transfer, interfacial synthesis, nonvolatile resistive memory device, organic electronics, polyimide*

1. INTRODUCTION

Resistive switching memories or memristors are recognized as the next-generation information storage and neuromorphic computing technologies due to the simple two-terminal device geometry, excellent miniaturization potential, versatile ranges of material selection, fast switching speed (within few nanoseconds), low energy consumption (sub-pico joule) and high switching endurance.[1-4] Benefiting from the atomic engineering and molecular design-synthesis strategy, organic materials with tunable electronic structures have increasingly drawn extensive attention for applications in resistive memories.[5-9] The lightweight, solution processability, low-cost fabrication, and versatile synthetic strategies render organic materials promising candidates to meet the needs of design and physical realization of novel resistive memory devices.[10,11] In this context, the intrinsic electronic and structural features of organic materials dominate the resistive switching behavior between two or more stable resistance states. A well-defined organic structure involved in resistive memory devices is essential to understanding the switching mechanism and developing high-performance resistive memory devices.

Two-dimensional covalent organic frameworks (2D COFs) are crystalline porous materials that feature the covalently connected networks and precisely layered stacking π-columns.[12,13] By virtue of the predictable topologies, ordered structures, high surface area, high stability, and tunable functionalities, 2D COFs have shown extensive potential applications in energy

storage, photoenergy conversion, catalysis, electronics, and optoelectronics.[14-19] The electronic properties of 2D COFs can be engineered by modifying the linking motifs and molecular properties of building blocks, typically rigid aromatic units.[20-23] A variety of 2D COF-based organic semiconductors have been constructed from conjugated molecules (such as pyrene, porphyrin, and phthalocyanine) to afford well-defined π-arrays with tunable charge transfer.[24-26] Among these, fusing the donor and acceptor moieties into 2D frameworks via direct polycondensation gives rise to robust COF materials with tunable electronic properties.[27,28]

Growing crystalline COF films at confined interfaces facilitated their integration into device-relevant settings such as field-effect transistors and photodetector devices.[29-33] Recently, an ultrathin 2D imine polymer film constructed from benzene-1,3,5-tricarbaldehyde and *p*-phenylenediamine was reported by Hu and Lei for a sandwiched non-volatile memristor based on the filament conductive mechanism taking advantages of the porous structure of the 2D polymer.[34] Park et al. reported the surfactant-assisted interfacial synthesis of crystalline 2D boronate ester COF films as the pseudo-gate for emulating the synaptic plasticity with silicon nanowire field-effect transistor in a neuromorphic memory device.[35] Despite these examples, integration of well-defined 2D COF films with tunable intrinsic charge transfer characteristics into two-terminal sandwiched resistive memory devices is underexplored yet.

2D polyimide COFs (PI-COFs) have been produced by the condensation between multi-amino monomers and dianhydrides.[36-39] Typically, polyimide materials possess high thermal stability (up to 535 °C), chemical resistance, and excellent properties.[36] Functional polyimide materials containing both electron donors and acceptors in a single conjugated skeleton can offer unique electronic transitions due to intramolecular charge transfer (ICT).[40,41] The highly ordered, segregated donor-on-donor and acceptor-on-acceptor alignment and inter-layer π–π interactions in 2D PI-COFs offer efficient pathways for the transport of photogenerated or electrically injected charge carriers.[37,38] These characters render 2D PI-COFs excellent candidates in the fields of energy storage, fluorescence sensing and electrochemical catalysis, but not in the fabrication of organic electronic devices.

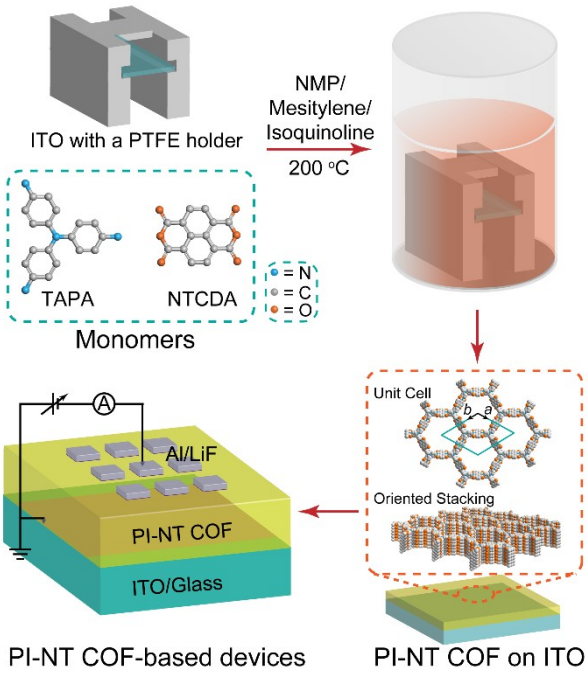

Figure 1. Schematic diagram of the solvothermal synthesis of PI-NT COF film on an ITO-coated glass substrate and the sketch of the resistive switching memory devices with the ITO/PI-NT COF film/LiF/Al configuration.

Herein, we demonstrated the first surface grown donor-acceptor (D-A) PI-NT COF films on ITO-coated glass substrates, employing the electron-donating 4,4',4''-triaminotriphenylamine (TAPA) and the electron-withdrawing naphthalene-1,4,5,8-tetracarboxylic dianhydride (NTCDA) as precursors in optimized solvothermal reactions (Figure 1). The crystalline and oriented PI-NT COF films were obtained via optimized solvothermal reactions, and then used to fabricate resistive memory devices Write-once-read-many-time (WORM) resistive switching memory behavior was recorded under the threshold switching voltage of +2.30 V for the positive scan and –2.64 V for the negative scan. A high ON/OFF current ratio (>10^6 for the positive scan and 10^4~10^6 for the negative scan) was obtained with high stability and long-term retention time. The resistive memory behavior was attributed to electric field-induced charge transfer, underscoring a novel approach to 2D COF-based information storage units. To the best of our knowledge, this is the first example that demonstrates the electrical resistive memory properties based on the intrinsic charge transfer characteristics of 2D COF films.

2. RESULTS AND DISCUSSION

2.1 Synthesis and Characterizations of PI-NT COF Films. Previously polyimide 2D COFs were synthesized in sealed glass tubes under solvothermal conditions, which showed high chemical and thermal stability compared to the imine-linked ones.[36-39] In the present work, the D-

A type PI-NT COF was designed by using the naphthalene diimide unit as electron acceptor and triaryl amine unit as electron donor. A well-defined D-A polyimide 2D COF could be constructed with novel electronic characteristics. Firstly, the solvothermal conditions for the synthesis of PI-NT COF powder in autoclave were optimized and the obtained powder was characterized (Figures S1-S5).

We found that PI-NT COF powder obtained from slightly modified literature conditions gave the best result, where 1-methyl-2-pyrrolidinone (NMP)/mesitylene (1:1 v/v) was used as the solvent and isoquinoline as the catalyst at 200 °C. The chemical identity and structural regularity of PI-NT COF powder were confirmed by FTIR spectroscopy, solid-state ^{13}C NMR spectroscopy and powder X-ray diffraction (PXRD). Based on the monomer structures and diimide bonding motifs, a 2D layered hexagonal topology was proposed for the simulated pattern. The Pawley refinement demonstrated that the AA stacking model gave the best fit, and the calculated unit cell parameters were obtained as $a = b = 32.2430$ Å, $c = 4.2758$ Å, $\alpha = \beta = 90°$, $\gamma = 120°$ with good residual factors ($R_{wp} = 4.73\%$ and $R_p = 3.47\%$). The diffraction peaks at 2.98°, 6.34°, 8.28°, and 20.94° using Cu Kα radiation (Figure S4) were indexed as the diffraction of (100), (200), (210) and (001) facets, respectively, corresponding to peaks at q_{xy} 0.21, 0.47, 0.61 and 1.54 Å^{-1} in the synchrotron PXRD pattern (Figure S5).

Then, PI-NT COF films were fabricated on an ITO-coated glass substrate via a solvothermal reaction by using a custom-designed PTFE holder in autoclave. The chemical formation of PI-NT COF films was confirmed by FTIR spectra in attenuated total reflectance mode (ATR-FTIR, Figure 2a). The stretching peaks of amino groups (in the range from 3300 to 3450 cm^{-1}) and anhydride C=O groups (around 1775 cm^{-1}) totally disappeared. The emerging characteristic peaks at 1716 and 1672 cm^{-1} were ascribed to the asymmetric stretching of imide C=O and the peak at 1348 cm^{-1} was attributed to the stretching mode of imide C-N-C,[36] supporting the formation of imide groups in PI-NT COF films. Varying the reaction time (1 day to 3 days) and monomer concentrations (1 mM to 4 mM based on TAPA) had a negligible impact on the FTIR spectra of PI-NT COF films (Figure S6), though the impact on crystallinity was obvious (see discussions later). The typical grazing incidence wide-angle X-ray scattering (GIWAXS) patterns were recorded for optimizing the conditions for thin films growth (Figures S7 and S8). As shown in the GIWAXS pattern under the optimal solvothermal conditions (Figure 2b), the diffraction peaks corresponding to (100), (200) and (210) facets were notably confined in the q_{xy} plane as indicated by the Bragg rods, while a broad and diffusive out-of-plane π-π stacking peak was found at around $q_z = 1.54$ Å^{-1}, indicating both decent crystallinity and good orientation preference of the PI-NT COF film with the 2D layers lying parallel to the substrate and the π-column stacking in the perpendicular direction. The crystallinity and orientation of PI-NT COF films showed a significant correlation to the monomer concentration. Lower monomer concentration (1 mM TAPA and 1.5 mM NTCDA) resulted in weak diffractions, while higher concentration (4 mM TAPA and 6 mM NTCDA) led to low orientation preference as indicated by the circular pattern of (200) diffraction peaks instead of Bragg rods (Figure S8). Moreover, the chemical structure and oriented crystallinity could be held for more than 6 months as stored in inert conditions, indicating the good stability of the PI-NT COF films.

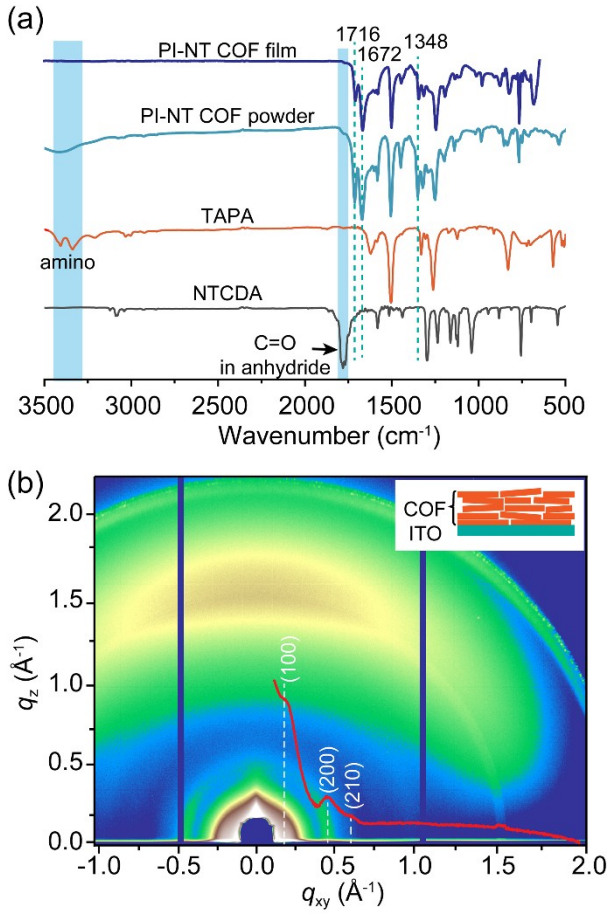

Figure 2. (a) Comparison of FTIR spectra of precursors, PI-NT COF film (ATR-FTIR), and powder. (b) Typical GIWAXS pattern of PI-NT COF film on ITO-coated glass substrate overlaid with the in-plane line profile plot (red curve). Inset: the stacking model of PI-NT COF films on ITO surface.

The surface roughness and thickness of the solvothermal synthesized PI-NT COF films were investigated by atomic force microscope (AFM). Flat PI-NT COF films consisting of nanoparticles (Figure S9) were obtained with a typical thickness of 38 ± 7 nm and surface roughness (*R*a) of 1.63 nm (Table S1) at 1 mM TAPA and 1.5 mM NTCDA. When doubling the monomer concentration, the

PI-NT COF films showed a dense and smooth surface despite few aggregated particles atop (Figures 3a and 3b). The film had a thickness of 102 ± 12 nm (Figure 3c) with a slightly increased surface *R*a of 2.26 nm. The film thickness increased to 274 ± 71 nm as increasing the monomer concentration to 4 mM TAPA and 6 mM NTCDA (Figure S10 and Table S1). A rugged surface was observed with large particles (the diameter is more than 200 nm) together with a higher *R*a value (54.6 nm).

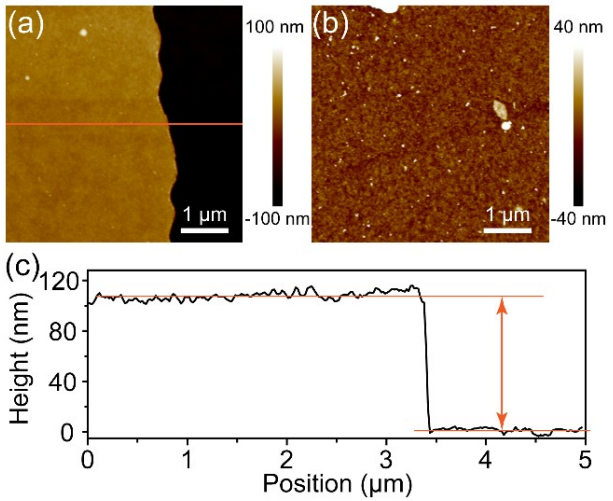

Figure 3. Topographic AFM images showing PI-NT COF film (edge (a) and surface (b)), and (c) cross-section height profile of PI-NT COF film (synthesized from 2 mM TAPA and 1.5 mM NTCDA in NMP/mesitylene (1:1 v/v) with isoquinoline at 200 °C for 3 days).

2.2 Resistive memory device and electronic performance. Two-terminal resistive memory devices were fabricated by thermally depositing aluminum pads (200 × 200 μm^2) with or without a buffer layer of LiF (1 nm) onto the surface of PI-NT COF film/ITO/glass using a copper grid as the shadow mask (Figure 1). The effect of film thickness on the resistive memory behavior was investigated. Our results demonstrated that the thickness (in the range of 90 to 150 nm) of crystalline PI-NT COF films has little impact on the resistive performance. The resistive memory performance of PI-NT COF films synthesized at lower concentration showed poor reproducibility. When the monomer concentration was increased to more than 4 mM TAPA and 6 mM NTCDA (Figure S10 and Table S1), a rugged surface was observed with large particles (the diameter was more than 200 nm), together with a higher Ra value (54.6 nm) and larger thickness. Taking the crystallinity, orientation, and topographical properties into consideration, the PI-NT COF films from 2 mM TAPA and 3 mM NTCDA were best suited for memory devices.

The typical devices remained in a high-resistance state (HRS, or OFF state) with a current less than 30 nA as the applied voltage swept in the window of –2 V to +2 V. When the external voltage was gradually swept from 0 to +3 V, an abrupt rise of current (up to 10 mA) was observed at the operating voltage of +2.29 V (Figure 4a, sweep 1), switching to a low-resistance state (LRS, or ON state). This conductivity change corresponded to the SET process of memory devices from the "0" state to the "1" state. The switching threshold voltages for various devices were on an average value of +(2.30 ± 0.17) V (Figure S11). The LRS was retained in the subsequent positive or negative sweeps (READ process, sweeps 2 and 3). Therefore, the ITO/PI-NT COF film/LiF/Al devices behaved as typical non-volatile write-once-read-many-times (WORM) memories.

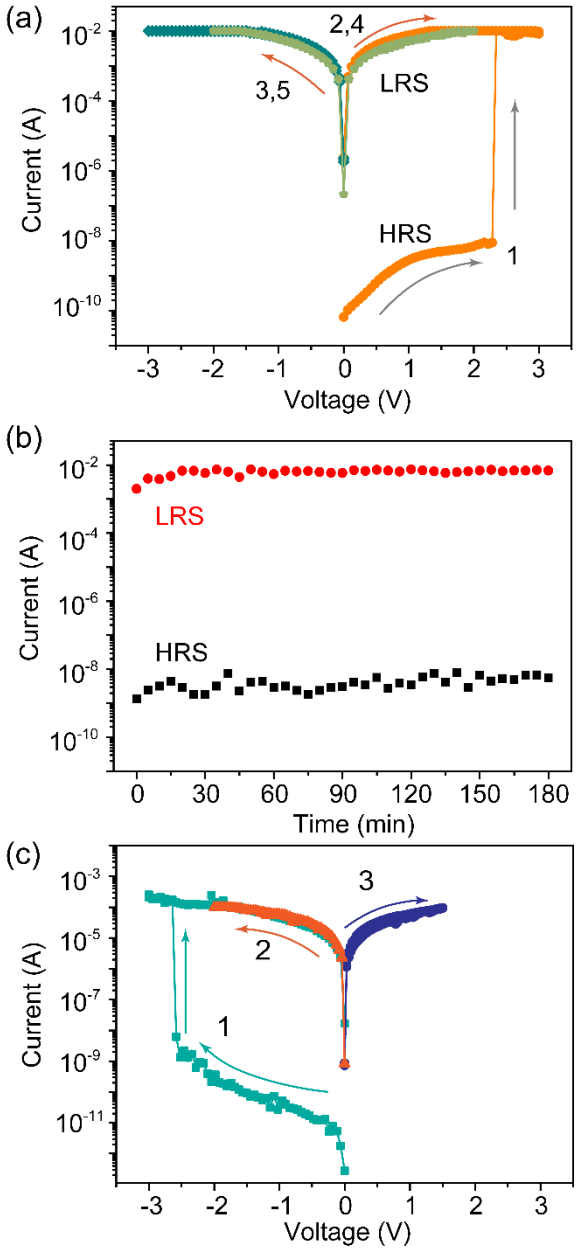

Figure 4. (a) Typical current-voltage (*I-V*) characteristics on the positive scan for the memory device. Sweep 1: from 0 V to +3 V; sweeps 2 and 4: from 0 V to +3 V and +2 V, respectively; sweeps 3

and 5: from 0 V to -3 V and -2 V, respectively. HRS and LRS represent high-resistance state and low-resistance state, respectively. (b) Retention characteristics for LRS and HRS at +1 V (READ) on the positive scan. (c) Typical *I-V* characteristics on the negative scan for memory devices. Sweep 1: from 0 V to –3 V; sweep 2: from 0 V to –2 V; sweep 3: reversing sweep between 0 V to +1.5 V.

A high ON/OFF current ratio (>10^6, up to 10^7 at +0.2 V) was obtained for the ITO/PI-NT COF film/LiF/Al devices on the positive scan by comparing the LRS current to the HRS one (Figure S12), a favorable feature that would facilitate reading and writing information with high fidelity and low errors. Our measurements demonstrated that the stable switching behavior can be obtained in the voltage window between –2 V and +2 V for the READ process (sweeps 4 and 5). The read current for both LRS and HRS under a constant voltage of +1 V can remain stable without any degradation for 180 min (namely, more than 10^4 s) at the ambient conditions, respectively (Figure 4b). The LRS can be held as measured even after 2 months. Our measurements also indicated that the ITO/PI-NT COF film/LiF/Al devices could be cycled for more than 200 times. These results indicate that the ITO/PI-NT COF film/LiF/Al devices are durable and feasible for the potential application in practical memory devices.

Negative scans can also reveal similar WORM resistive switching behavior as shown in Figure 4c. A slightly higher switching threshold voltage of –(2.64 ± 0.12) V was recorded (sweep 1). The LRS current at the level of ~10^{-4} A at the operating voltage of –1 V was remarkably lower than that of the positive scan and could remain stable as sweeping the READ voltage in the range of –2 V to +1.5 V (sweeps 2 and 3). The current ON/OFF ratios in a wider range of ~10^4 to ~10^6 is obtained due to the varying HRS current levels (Figure S13). These results are comparable to the previous resistive memory devices based on imide-type D-A small molecules and polymers (see Table S2 for details).

To understand the effect of ordered D-A stacking structure to the memristor performance, the PI-NT amorphous film (Figure S14) based devices (ITO/PI-NT amorphous film/LiF/Al) were prepared and tested. WORM behavior was recorded on the positive scan with a threshold of around +2 V but demonstrating a higher HRS current (microampere level) and lower current ON/OFF ratio (~10^4 at +1 V, Figure S15a). The negative scan also showed WORM property with a poor LRS current and ON/OFF ratio (~0.1 mA and 10^2 at –1 V, respectively, Figure S15b). These resistive switching characteristics showed poor reproducibility and low stability, indicating that the crystallinity and orientation of PI-NT COF films rendered the resistive memory devices excellent performance.

Our control results demonstrated that the LiF layer played an important role in the stable non-volatile resistive memory devices. As we applied the voltage on the ITO/PI-NT COF film/Al devices that were free of LiF layers, the resistive switching behavior was also observed but only on the negative scan (Figure S16). The HRS with higher current (~10 μA at –1 V) was turned to the LRS at around –3.11 V, showing a current ON/OFF ratio of ~10^2 at –1 V. When the applied voltage was in the range of –4 V to +2 V, the similar WORM drive patterns were recorded and the LRS could be read for more than 10^3 s. Further higher positive bias would annihilate the charge transfer channels and turn LRS to HRS at +3.90 V on the positive scan. Unfortunately, only a few ITO/PI-NT COF film/Al device worked well, and these devices couldn't be turned on again once they were switched off on an external positive scan, indicating the poor reproducibility and volatile memory behavior for such devices.

By comparing the performance of PI-NT COF film-based resistive switching memory devices with or without LiF buffer layer, it suggests that a nanometer-thick buffer layer of LiF is conducive to enhancing the WORM memory performance of the COF-based devices with enhanced ON/OFF current ratio and stability, presumably by avoiding direct contact between the metal electrodes and the organic films and improving the interface barrier for charge injection and migration between Al electrodes and PI-NT COF films.[42,43] Due to the intrinsic insulating property of LiF, a thicker LiF buffer layer (>5 nm) led to ultralow current and no resistance switching behavior. Moreover, LiF layer is also helpful in preventing the formation of conductive metal filaments in organic layers (see more discussions later).

2.3 Physical characteristics and mechanism of resistive memory behaviors. The resistive memory behavior is attributed to the switching characteristics in different stable resistance states, which mainly originate from the formed filament or electric-induced charge transfer.[10] To verify the possibility of filament mechanism, element distribution across the switched memory device in its LRS was measured by TEM after being tested for more than 10^4 s (Figure 5a). The cross-section TEM sample slices were prepared by depositing a protective Pt layer at the top, followed by slicing with a micro/nano-operating platform equipped with FIB and electron beam. The top Pt layer and the bottom ITO layers were clearly visible in the elemental mapping. In between were the Al electrode layer and the active COF layer, as revealed by the Al and carbon element map. Importantly, the Al map illustrated that the Al element was only confined in the Al electrode layer, with no signs of permeation into the underneath COF layer. The lack of Al filaments in the PI-NT COF films provided strong evidence to rule out electrode

filament growth as the mechanism for conductivity switching, which had been observed in previously reported 2D polyimine film memristors and other organic memories.[34,44,45]

The possible switching mechanism was elucidated based on the D-A structure of PI-NT COF. The UV-vis absorption spectra (Figure 5b) of PI-NT COF films revealed strong absorbance in the UV region and a broad absorption feature extended well across the visible region, the latter being quite distinct from these of the monomers (TAPA and NTCDA). A broad absorption, peaked around 520 nm, was attributable to the formation of $NTCDA^{-\bullet}/TAPA^{+\bullet}$ charge transfer complex in the PI-NT COF.[37] The lowest unoccupied molecular orbit (LUMO) and the highest occupied molecular orbit (HOMO) energy levels were estimated to be –3.62 eV and –5.09 eV, respectively, derived from the cyclic voltammetry curve in Figure S17, which was comparable to the molecular orbital calculations (E_{HOMO} = –5.52 eV and E_{LUMO} = –3.65 eV) according to the previous report.[37] The bandgap (1.47 eV) is comparable to the optical one (1.82 eV, evaluated from Tauc's plot as shown in Figure S18). The HOMO mainly concentrated on the TAPA cores, while the LUMO was confined in naphthalene diimide moieties (Figure S19). The band diagram of the PI-NT COF film and the relative energy levels with respect to ITO and Al/LiF electrodes were summarized in Figure 5c.

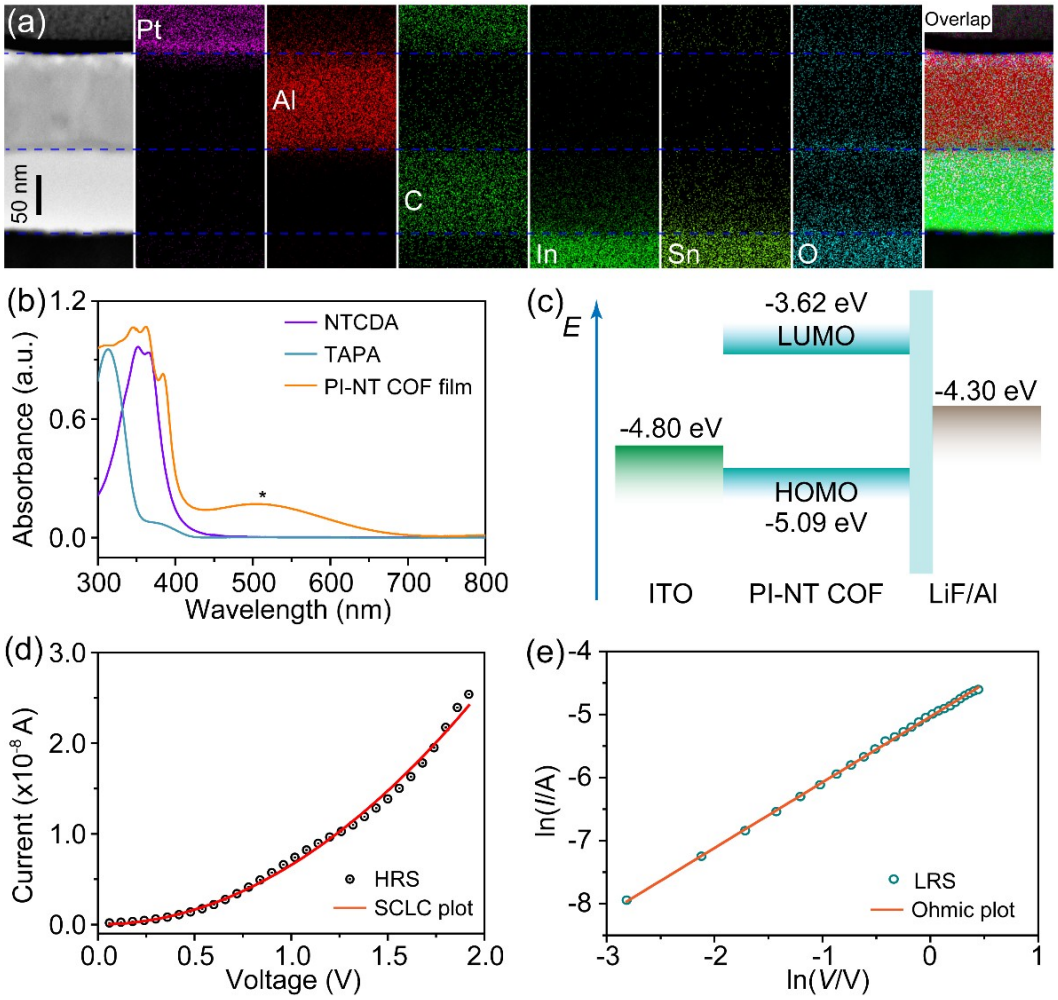

Figure 5. (a) TEM image and element distribution maps of a cross-section slice of an ITO/PI-NT COF film/LiF/Al memory device in its LRS. The cross-section slice sample was prepared via FIB with a Pt protective layer deposited on top. (b) UV-visible absorption spectra of PI-NT COF film, TAPA, and NTCDA. (c) Band diagrams and relative levels of PI-NT COF films compared to ITO and Al/LiF electrodes. (d) Space charge limited current (SCLC) fitting plot for voltage scan from 0 V to +2 V in the HRS. (e) ln*I* versus ln*V* plot in the LRS.

The dipole moment between TPA cores and NTCDA moieties in PI-NT COF was calculated to be 1.217 Debye by using density function theory (DFT) method, which was smaller than that of TPA-NDI molecule (2.506 Debye).[46] The medium dipole moment could hold the HRS without electric field. Under forward electric field, the ICT process from donor (TPA) cores to acceptor (NTCDA) moieties would result in the localization of electrons in LUMO and holes in HOMO, forming stable charge transfer channels. The separated HOMO and LUMO distribution of PI-NT COF could

stabilize the charge transfer channel and carrier trapping environment after turning off the power, leading to quasi-permanent LSR shown in PI-NT COF-based WORM devices.

The electric-field-induced ICT process and charge carrier migration were also illustrated based on the *I*-*V* characteristics which were separately replotted for the HRS and LRS (Figures 5d and 5e). The *I*-*V* curve in the HRS could be fitted by using the space-charge limited current (SCLC) model with a correlation coefficient of 0.996 (Figure 5d). In order to illustrate the conductive mechanism at HRS, the ln*I*-ln*V* curve was employed. The slope (*m*) of linear region in ln*I*-ln*V* curve derived from the power law $I \propto V^m$ imply the specific characters in each region.[47] There were two linear regions in the ln*I*-ln*V* curve at HRS on the positive scan (Figure S20) with the slopes of 0.91 and 1.96, which represented the Ohmic and SCLC transport characteristics, respectively. These results implied that the HRS was dominated by the SCLC conductance.[48] For the positive scan, the hole transporting rather than electrons was expected to dominate the memory behavior due to the large electron injection energy barrier (~1.18 eV) between the work function of ITO and the LUMO energy level. The charges (holes) injected from top Al electrodes with decreased barrier through the LiF buffer layer would be captured by the trapping centers (donating cores) near the electrodes. These trapped charges could not escape from the trapping sites which were confined by the induced countering space charges. As the applied voltage (threshold voltage around +2.38 V) is enough to drive the ICT in PI-NT COF films, the charge separation state in the D-A frameworks would break the trapping state and the injected charges can migrate effectively through the ordered charge transport channels with a lower resistance (namely, switching to the LRS). As the HRS is switched to the LRS, the linear relationship is observed both in the plots of ln(*I*/*V*) versus $V^{0.5}$ (Figure S21) and ln*I* versus ln*V* (slope ~1.05, Figure 5e), which suggests the trap-assisted Poole-Frenkel (PF) emission across the electrode-organic interface and the Ohmic conductance in the trap-free junction, respectively, demonstrating that the LRS current is dominated by the bulk charge transfer rather than the interfacial injection.[48,49] Similar electron transport characteristics were observed during the negative scan, as revealed by the SCLC plots in Figures S22–S25, despite higher threshold voltages and lower LRS currents that were attributable to the relatively large barrier for electron injection. Overall, the segregated HOMO and LUMO distributions and efficient ICT interactions in the D-A frameworks of PI-NT COF facilitate the formation of stable charge separation state and ordered charge percolation pathways, which contributes to the excellent non-volatile WORM memory property.

3. Conclusions

In summary, well-defined PI-NT COF films with ordered D-A arrangement were designed and synthesized on the ITO-coated glass substrates via a facile solvothermal reaction. The PI-NT COF films demonstrated ordered crystalline structure, good face-on crystallite orientation preference, and smooth surface from the optimized reaction conditions. Two-terminal sandwich-like devices were fabricated by depositing Al electrodes with a LiF interlayer and showed the typical non-volatile WORM memory property for both the positive and negative scans with the threshold voltage of +(2.30 ± 0.17) V and –(2.64 ± 0.12) V, respectively. The origin of the resistive switching behaviors was ascribed to a charge transfer mechanism under an external electric field, which was facilitated by the effective ICT and stable charge separation states in the D-A COF thin films. The high ON/OFF ratio (over 10^6), long-term retention time (>10^4 s) and good reproducibility associated with the memory devices suggest the great potential of well-defined D-A 2D COFs as active materials for high-performance data-storage devices with low error, high fidelity and durability.

4. Experimental Methods

4.1 Reagents and Materials. All chemicals and solvents were commercially available and used without any purification. 4,4',4''-Triaminotriphenylamine (TAPA, 4 mM, 97%), naphthalene-1,4,5,8-tetracarboxylic dianhydride (NTCDA), 1-methyl-2-pyrrolidinonewere (NMP, ACS reagent, ≥99%), mesitylene (98%), isoquinoline (97%) and Ferrocene (Fc) were purchased from Sigma-Aldrich Chemicals. Tetrahydrofuran (THF), acetone and isopropanol were obtained from Fisher Chemicals. The indium tin oxide (ITO) coated glasses were supplied by Thin Film Devices with an ITO layer thickness of 150 nm and a resistivity of 20 ohms per square.

4.2 Synthesis of PI-NT-COF films on ITO substrate. The interfacial growth of PI-NT-COF films on the ITO surface was carried out via a facile solvothermal method. Typically, TAPA (4 mM, 6 mL in NMP/mesitylene v/v = 1:1), NTCDA (6 mM, 6 mL in NMP/mesitylene v/v = 1:1) and isoquinoline (0.6 mL) were charged into a liner polytetrafluoroethylene (PTFE) autoclave (38 mL in total capacity). The homogeneous solution was ultrasonically treated for 5 min and then deaerated with inert nitrogen gas for 15 min. The ITO slices as the substrate for PI-NT-COF film growth were ultrasonically cleaned for 10 min by using soapy water, deionized water, acetone, and isopropanol in turn, dried in an oven at 120 °C for 4 h, and were subsequently loaded to a homemade Π-shaped PTFE holder (as shown in Figure 1) with conductive ITO side facing down. The PTFE holder with ITO slices was carefully submerged into the PTFE autoclave charged with the precursor solution. Then, the PTFE autoclave

was sealed in a stainless-steel container and heated to 200 °C for a certain time. After cooling down to room temperature, the ITO slices coated with PI-NT-COF films were rinsed with NMP, activated in THF overnight, and dried under vacuum.

4.3 Resistive memory device fabrication and measurements. The resistive memory devices were fabricated by depositing the top electrodes on the PI-NT-COF films grown on the ITO surface. The top electrodes (LiF/Al 1/80 nm or Al 80 nm) were deposited in an MBRAUN thermal evaporator under vacuum conditions of 2×10^{-4} mbar by using copper grids (100-mesh, a pore size of 200×200 μm^2, purchased from Electron Microscopy Sciences) as masks. The electronic performance of the fabricated resistive memory devices was investigated at ambient conditions by using an Agilent 4155C parameter analyzer integrated with a desktop EasyEXPERT software and a Lakeshore CPX-HF probe station equipped with 4 manipulated tungsten probes (25-micron tip radius). The cross-section transmission electron microscopic (TEM) slices sample of tested PI-NT-COF film-based resistive memory devices were prepared on a FEI Helios NanoLab G3 CX dual beam Focused Ion Beam (FIB) platform and tested in a JEM-2100F transmission electron microscope (TEM) equipped with an Oxford Aztec energy dispersive spectrometer (EDS) detector.

4.4 Characterization. Powder X-ray diffraction (PXRD) patterns were recorded at ambient temperature on a PANalytical Empyrean X-ray diffractometer with Cu Kα radiation (λ = 1.5416 Å), operated at 40 kV and 40 mA ranging from 1.5 to 40° with a speed of 1° min^{-1}. Two-dimensional X-ray scattering patterns (in transmission mode) and grazing incidence wide-angle X-ray scattering (GIWAXS, the incident angle chosen was 0.16 degrees) patterns were conducted at Beamline 7.3.3 at the Advanced Light Source (ALS), Lawrence Berkeley National Laboratory, using an approximately 10 keV X-ray beam (λ = 1.2398 Å). The sample-detector distance and beam-center positions were calibrated using silver behenate (AgB) standard sample. The patterns were analyzed by using the NIKA software package developed by J. Ilavsky. The chemical structure of PI-NT-COF powders was confirmed by Fourier transform infrared (FTIR) spectra obtained on a Perkin Elmer Spectrum One FTIR system, and solid-state ^{13}C NMR spectra recorded on a Bruker AVANCE III 400 M NMR spectrometer, respectively. FTIR spectra of PI-NT-COF films were recorded on a Thermo-Fisher Scientific Nicolet iS50 instrument using a germanium crystal attenuated total reflectance (ATR) mode with an additional variable angle reflectance accessory by Pike (VariGATR) after the measurement system being cooled with liquid nitrogen for 20 min. The solid-state UV-vis spectra were obtained on a Cary 5000 UV-Vis-NIR spectrometer from 300–800 nm in transmission mode referring to blank ITO glass. The cyclovoltammetry curves in the range of −2.5 V to +2 V were acquired on a Metrohm Autolab PGSTA302A electrochemical station in degassed anhydrous acetonitrile containing 0.1 M Bu_4NPF_6 at a scan rate of 50 mV s^{-1}. A typical three-electrode system was used where Ag/Ag^+ electrode (filled with 0.01 M $AgNO_3$ and 0.1 M Bu_4NPF_6 in anhydrous acetonitrile) served as the reference electrode (being calibrated to the redox potential of Fc/Fc^+), Pt wire as the auxiliary electrode and ITO slice coated with PI-NT-COF film as the working electrode. The surface topographic images and cross-section height analysis of PI-NT-COF films were performed on a Bruker Dimension Icon Atomic Force Microscope (AFM) with peak force tapping mode.

4.5 Crystal Structure modeling and refinements. The crystal models for PI-NT-COF were modeled by using Materials Studio 5.0 software package (Accelrys Software Inc. (2009, now BIOVIA). Materials Studio 5.0: Modeling Simulation for Chemical and Material, San Diego, CA.). The lattice parameters and atomic positions were optimized under the universal force field, and were further refined through the Pawley PXRD refinement conducted with the Reflex module until the R_{wp} value converging and a good agreement obtained between the refined profiles and the experimental ones. The parameters including peak broadening, peak asymmetry, and zero shift error were considered in the applied Pseudo-Voigt profile function for whole profile refinement. The refined atomic coordinates of PI-NT-COF crystal structure models and space group models are presented in Table S3 and S4.

ASSOCIATED CONTENT

Supporting Information. The Supporting Information is available free of charge on the ACS Publications website at DOI:

Supplementary characterization of PI-NT COF film including FTIR spectra, PXRD patterns, solid-state ^{13}C-NMR spectrum, and AFM topographic images; additional resistive switching performance of COF-based memory devices; comparison of resistive memory performance to the previous works. Figure S1 to S25, Table S1 to S4. (PDF)

AUTHOR INFORMATION

Corresponding Author

* Yi Liu: yliu@lbl.gov; Bing Sun: sunbing@cugb.edu.cn; Dong Wang: wangd@iccas.ac.cn

ORCID:

Bing Sun: 0000-0001-5917-3094
Songliang Cai: 0000-0002-5399-9036
Jian Zhang: 0000-0003-0274-0814
Dong Wang: 0000-0002-1649-942X
Yi Liu: 0000-0002-3954-6102

Notes

The authors declare no competing financial interest.

ACKNOWLEDGMENT

This work was performed as a user project at the Molecular Foundry and Advanced Light Source, Lawrence Berkeley National Laboratory, both being supported by the Office of Science, Office of Basic Energy Sciences of the U.S. Department of Energy under contract No. DE-AC02-05CH11231. This work was also supported by the National Natural Science Foundation of China (Grant numbers 21802128, 21725306 and 21872154), the Strategic Priority Research Program of the Chinese Academy of Sciences (Grant No. XDB12020100), and the National Key R&D Program of China (2017YFA0204702). B.S. acknowledges the support from the China Scholarship Council (CSC) for his stay at Lawrence Berkeley National Laboratory. We thank Mrs. Liana M. Klivansky and Mr. Christopher L. Anderson from the Molecular Foundry for their help on film characterizations. We appreciate Dr. Jian Liu and the Electron Microscopy Group in Institute of Chemistry, Chinese Academy of Sciences (ICCAS) for their assistance on TEM measurements. We also thank Prof. Lang Jiang and Dr. Jie Liu from ICCAS for their kind help on device characterization.

REFERENCES

(1) Strukov, D. B.; Snider, G. S.; Stewart, D. R.; Williams, R. S. The Missing Memristor Found. *Nature* **2008,** *453*, 80-83.

(2) Wang, M.; Cai, S.; Pan, C.; Wang, C.; Lian, X.; Zhuo, Y.; Xu, K.; Cao, T.; Pan, X.; Wang, B.; Liang, S.-J.; Yang, J. J.; Wang, P.; Miao, F. Robust Memristors Based on Layered Two-Dimensional Materials. *Nat. Electron.* **2018,** *1*, 130-136.

(3) Wang, Z.; Joshi, S.; Savel'ev, S. E.; Jiang, H.; Midya, R.; Lin, P.; Hu, M.; Ge, N.; Strachan, J. P.; Li, Z.; Wu, Q.; Barnell, M.; Li, G.-L.; Xin, H. L.; Williams, R. S.; Xia, Q.; Yang, J. J. Memristors with Diffusive Dynamics as Synaptic Emulators for Neuromorphic Computing. *Nat. Mater.* **2016,** *16*, 101-108.

(4) Chua, L. Resistance Switching Memories Are Memristors. *Appl. Phys. A* **2011,** *102*, 765-783.

(5) Cho, B.; Song, S.; Ji, Y.; Kim, T.-W.; Lee, T. Organic Resistive Memory Devices: Performance Enhancement, Integration, and Advanced Architectures. *Adv. Funct. Mater.* **2011,** *21*, 2806-2829.

(6) Wang, C.; Gu, P.; Hu, B.; Zhang, Q. Recent Progress in Organic Resistance Memory with Small Molecules and Inorganic-Organic Hybrid Polymers as Active Elements. *J. Mater. Chem. C* **2015,** *3*, 10055-10065.

(7) Gu, P.-Y.; Zhou, F.; Gao, J.; Li, G.; Wang, C.; Xu, Q.-F.; Zhang, Q.; Lu, J.-M. Synthesis, Characterization, and Nonvolatile Ternary Memory Behavior of a Larger Heteroacene with Nine Linearly Fused Rings and Two Different Heteroatoms. *J. Am. Chem. Soc.* **2013,** *135*, 14086-14089.

(8) Li, Y.; Zhang, C.; Li, Z.; Gu, P.; Wang, Z.; Li, H.; Lu, J.; Zhang, Q. Controlled Deposition of Large-Area and Highly Ordered Thin Films: Effect of Dip-Coating-Induced Morphological Evolution on Resistive Memory Performance. *J. Mater. Chem. C* **2019,** *7*, 3512-3521.

(9) Liu, J.; Jiang, L.; Hu, W.; Liu, Y.; Zhu D. Monolayer Organic Field-Effect Transistors. *Sci. China. Chem*., **2019**, *62*, 313–330.

(10) Gao, S.; Yi, X.; Shang, J.; Liu, G.; Li, R. W. Organic and Hybrid Resistive Switching Materials and Devices. *Chem. Soc. Rev.* **2019,** *48*, 1531-1565.

(11) Zhao, K.; Yu, F.; Liu, W.; Huang, Y.; Said, A. A.; Li, Y.; Zhang, Q. Unexpected Synthesis, Properties, and Nonvolatile Memory Device Application of Imidazole-Fused Azaacenes. *J. Org. Chem.* **2020,** *85*, 101-107.

(12) Huang, N.; Wang, P.; Jiang, D. Covalent Organic Frameworks: A Materials Platform for Structural and Functional Designs. *Nat. Rev. Mater.* **2016,** *1*, 16068.

(13) Lohse, M. S.; Bein, T. Covalent Organic Frameworks: Structures, Synthesis, and Applications. *Adv. Funct. Mater.* **2018,** *28*, 1705553.

(14) Lin, C. Y.; Zhang, D.; Zhao, Z.; Xia, Z. Covalent Organic Framework Electrocatalysts for Clean Energy Conversion. *Adv. Mater.* **2018,** *30*, 1703646.

(15) Sick, T.; Hufnagel, A. G.; Kampmann, J.; Kondofersky, I.; Calik, M.; Rotter, J. M.; Evans, A.; Doblinger, M.; Herbert, S.; Peters, K.; Bohm, D.; Knochel, P.; Medina, D. D.; Fattakhova-Rohlfing, D.; Bein, T. Oriented Films of Conjugated 2D Covalent Organic Frameworks as Photocathodes for Water Splitting. *J. Am. Chem. Soc.* **2018,** *140*, 2085-2092.

(16) Diercks, C. S.; Lin, S.; Kornienko, N.; Kapustin, E. A.; Nichols, E. M.; Zhu, C.; Zhao, Y.; Chang, C. J.; Yaghi, O. M. Reticular Electronic Tuning of Porphyrin Active Sites in Covalent Organic Frameworks for Electrocatalytic Carbon Dioxide Reduction. *J. Am. Chem. Soc.* **2018,** *140*, 1116-1122.

(17) Ma, L.; Wang, S.; Feng, X.; Wang, B. Recent Advances of Covalent Organic Frameworks in Electronic and Optical Applications. *Chin. Chem. Lett.* **2016,** *27*, 1383-1394.

(18) Banerjee, T.; Gottschling, K.; Savasci, G.; Ochsenfeld, C.; Lotsch, B. V. H_2 Evolution with Covalent Organic Framework Photocatalysts. *ACS Energy Lett.* **2018,** *3*, 400-409.

(19) Sun, T.; Xie, J.; Guo, W.; Li, D.-S.; Zhang, Q. Covalent–Organic Frameworks: Advanced Organic Electrode Materials for Rechargeable Batteries. *Adv. Energy Mater.* **2020,** *10*, 1904199.

(20) Meng, Z.; Stolz, R. M.; Mirica, K. A. Two-Dimensional Chemiresistive Covalent Organic Framework with High Intrinsic Conductivity. *J. Am. Chem. Soc.* **2019,** *141*, 11929-11937.

(21) Lyu, H.; Diercks, C. S.; Zhu, C.; Yaghi, O. M. Porous Crystalline Olefin-Linked Covalent Organic Frameworks. *J. Am. Chem. Soc.* **2019,** *141*, 6848-6852.

(22) Jin, E.; Asada, M.; Xu, Q.; Dalapati, S.; Addicoat, M. A.; Brady, M. A.; Xu, H.; Nakamura, T.; Heine, T.; Chen, Q.; Jiang, D. Two-Dimensional sp^2 Carbon-Conjugated Covalent Organic Frameworks. *Science* **2017,** *357*, 673-676.

(23) Bi, S.; Yang, C.; Zhang, W.; Xu, J.; Liu, L.; Wu, D.; Wang, X.; Han, Y.; Liang, Q.; Zhang, F. Two-Dimensional Semiconducting Covalent Organic Frameworks via Condensation at Arylmethyl Carbon Atoms. *Nat. Commun.* **2019,** *10*, 2467.

(24) Joshi, T.; Chen, C.; Li, H.; Diercks, C. S.; Wang, G.; Waller, P. J.; Li, H.; Bredas, J. L.; Yaghi, O. M.; Crommie, M. F. Local Electronic Structure of Molecular Heterojunctions in a Single-Layer 2D Covalent Organic Framework. *Adv. Mater.* **2019,** *31*, e1805941.

(25) Rizzo, D. J.; Dai, Q.; Bronner, C.; Veber, G.; Smith, B. J.; Matsumoto, M.; Thomas, S.; Nguyen, G. D.; Forrester, P. R.; Zhao, W.; Jorgensen, J. H.; Dichtel, W. R.; Fischer, F. R.; Li, H.; Bredas, J. L.; Crommie, M. F. Revealing the Local Electronic Structure of a Single-Layer Covalent Organic Framework through Electronic Decoupling. *Nano Lett.* **2020,** *20*, 963-970.

(26) Chen, C.; Joshi, T.; Li, H.; Chavez, A. D.; Pedramrazi, Z.; Liu, P. N.; Li, H.; Dichtel, W. R.; Bredas, J. L.; Crommie, M. F. Local Electronic Structure of a Single-Layer Porphyrin-Containing Covalent Organic Framework. *ACS Nano* **2018,** *12*, 385-391.
(27) Jin, S.; Supur, M.; Addicoat, M.; Furukawa, K.; Chen, L.; Nakamura, T.; Fukuzumi, S.; Irle, S.; Jiang, D. Creation of Superheterojunction Polymers via Direct Polycondensation: Segregated and Bicontinuous Donor-Acceptor π-Columnar Arrays in Covalent Organic Frameworks for Long-Lived Charge Separation. *J. Am. Chem. Soc.* **2015,** *137*, 7817-7827.
(28) Medina, D. D.; Sick, T.; Bein, T. Photoactive and Conducting Covalent Organic Frameworks. *Adv. Energy Mater.* **2017,** *7*, 1700387.
(29) Wang, H.; Zeng, Z.; Xu, P.; Li, L.; Zeng, G.; Xiao, R.; Tang, Z.; Huang, D.; Tang, L.; Lai, C.; Jiang, D.; Liu, Y.; Yi, H.; Qin, L.; Ye, S.; Ren, X.; Tang, W. Recent Progress in Covalent Organic Framework Thin Films: Fabrications, Applications and Perspectives. *Chem. Soc. Rev.* **2019,** *48*, 488-516.
(30) Hao, Q.; Li, Z. J.; Lu, C.; Sun, B.; Zhong, Y. W.; Wan, L. J.; Wang, D. Oriented Two-Dimensional Covalent Organic Framework Films for Near-Infrared Electrochromic Application. *J. Am. Chem. Soc.* **2019,** *141*, 19831-19838.
(31) Medina, D. D.; Petrus, M. L.; Jumabekov, A. N.; Margraf, J. T.; Weinberger, S.; Rotter, J. M.; Clark, T.; Bein, T. Directional Charge-Carrier Transport in Oriented Benzodithiophene Covalent Organic Framework Thin Films. *ACS Nano* **2017,** *11*, 2706-2713.
(32) Sun, B.; Zhu, C.-H.; Liu, Y.; Wang, C.; Wan, L.-J.; Wang, D. Oriented Covalent Organic Framework Film on Graphene for Robust Ambipolar Vertical Organic Field-Effect Transistor. *Chem. Mater.* **2017,** *29*, 4367-4374.
(33) Xiong, Y.; Liao, Q.; Huang, Z.; Huang, X.; Ke, C.; Zhu, H.; Dong, C.; Wang, H.; Xi, K.; Zhan, P.; Xu, F.; Lu, Y. Ultrahigh Responsivity Photodetectors of 2D Covalent Organic Frameworks Integrated on Graphene. *Adv. Mater.* **2020,** *32*, e1907242.
(34) Liu, J.; Yang, F. X.; Cao, L. L.; Li, B. L.; Yuan, K.; Lei, S. B.; Hu, W. P. A Robust Nonvolatile Resistive Memory Device Based on a Freestanding Ultrathin 2D Imine Polymer Film. *Adv. Mater.* **2019,** *31*, e1902264.
(35) Park, S.; Liao, Z.; Ibarlucea, B.; Qi, H.; Lin, H. H.; Becker, D.; Melidonie, J.; Zhang, T.; Sahabudeen, H.; Baraban, L.; Baek, C. K.; Zheng, Z.; Zschech, E.; Fery, A.; Heine, T.; Kaiser, U.; Cuniberti, G.; Dong, R.; Feng, X. Two-Dimensional Boronate Ester Covalent Organic Framework Thin Films with Large Single Crystalline Domains for a Neuromorphic Memory Device. *Angew. Chem. Int. Ed.* **2020**, 10.1002/anie.201916595.
(36) Fang, Q.; Zhuang, Z.; Gu, S.; Kaspar, R. B.; Zheng, J.; Wang, J.; Qiu, S.; Yan, Y. Designed Synthesis of Large-Pore Crystalline Polyimide Covalent Organic Frameworks. *Nat. Commun.* **2014,** *5*, 4503.
(37) Lv, J. Q.; Tan, Y. X.; Xie, J. F.; Yang, R.; Yu, M. X.; Sun, S. S.; Li, M. D.; Yuan, D. Q.; Wang, Y. B. Direct Solar-to-Electrochemical Energy Storage in a Functionalized Covalent Organic Framework. *Angew. Chem. Int. Ed.* **2018,** *57*, 12716-12720.
(38) Kim, T. W.; Jun, S.; Ha, Y.; Yadav, R. K.; Kumar, A.; Yoo, C. Y.; Oh, I.; Lim, H. K.; Shin, J. W.; Ryoo, R.; Kim, H.; Kim, J.; Baeg, J. O.; Ihee, H. Ultrafast Charge Transfer Coupled with Lattice Phonons in Two-Dimensional Covalent Organic Frameworks. *Nat. Commun.* **2019,** *10*, 1873.
(39) Jiang, L.; Tian, Y.; Sun, T.; Zhu, Y.; Ren, H.; Zou, X.; Ma, Y.; Meihaus, K. R.; Long, J. R.; Zhu, G. A Crystalline Polyimide Porous Organic Framework for Selective Adsorption of Acetylene over Ethylene. *J. Am. Chem. Soc.* **2018,** *140*, 15724-15730.
(40) Toma, F. M.; Puntoriero, F.; Pho, T. V.; La Rosa, M.; Jun, Y. S.; Tremolet de Villers, B. J.; Pavlovich, J.; Stucky, G. D.; Campagna, S.; Wudl, F. Polyimide Dendrimers Containing Multiple Electron Donor-Acceptor Units and Their Unique Photophysical Properties. *Angew. Chem. Int. Ed.* **2015,** *54*, 6775-6779.
(41) Liu, C.-L.; Chen, W.-C. Donor–Acceptor Polymers for Advanced Memory Device Applications. *Polym. Chem.* **2011,** *2*, 2169–2174.
(42) Zhang, Q.; He, J.; Zhuang, H.; Li, H.; Li, N.; Xu, Q.; Chen, D.; Lu, J. Rational Design of Small Molecules to Implement Organic Quaternary Memory Devices. *Adv. Funct. Mater.* **2016,** *26*, 146-154.
(43) Hung, L. S.; Tang, C. W.; Mason, M. G. Enhanced Electron Injection in Organic Electroluminescence Devices Using an Al/LiF Electrode. *Appl. Phys. Lett.* **1997,** *70*, 152-154.
(44) Lee, B.-H.; Bae, H.; Seong, H.; Lee, D.-I.; Park, H.; Choi, Y. J.; Im, S.-G.; Kim, S. O.; Choi, Y.-K. Direct Observation of a Carbon Filament in Water-Resistant Organic Memory. *ACS Nano* **2015,** *9*, 7306-7313.
(45) Krishnan, K.; Tsuruoka, T.; Mannequin, C.; Aono, M. Mechanism for Conducting Filament Growth in Self-Assembled Polymer Thin Films for Redox-Based Atomic Switches. *Adv. Mater.* **2016,** *28*, 640-648.
(46) Lai, C.-H.; Muhammad, S.; Al-Sehemi, A. G.; Chaudhry, A. R. A Systematic Study of the Effects of Thionation in Naphthalene Dimide Derivatives to Tune Their Nonlinear Optical Properties. *J. Mol. Graph. Model.*, **2019**, *87*, 68-75.
(47) Dey, A.; Middya, S.; Jana, R.; Das, M.; Datta, J.; Layek, A.; Ray, P. P. Light Induced Charge Transport Property Analysis of Nanostructured ZnS Based Schottky Diode. *J. Mater. Sci.: Mater. Electron.* **2016**, *27*, 6325-6335.
(48) Wu, H.-C.; Zhang, J.; Bo, Z.; Chen, W.-C. Well-Defined Star-Shaped Donor–Acceptor Conjugated Molecules for Organic Resistive Memory Devices. *Chem. Commun.* **2015,** *51*, 14179-14182.
(49) Zhang, P.; Xu, B.; Gao, C.; Chen, G.; Gao, M. Facile Synthesis of Co_9Se_8 Quantum Dots as Charge Traps for Flexible Organic Resistive Switching Memory Device. *ACS Appl. Mater. Interfaces* **2016,** *8*, 30336-30343.

Table of Contents artwork

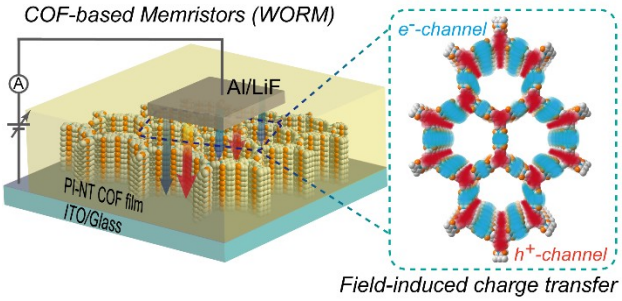

82 mm × 40 mm 600 dpi